Editors' Suggestion

Low-temperature magnetism of $KAgF_3$

John M. Wilkinson [1,2,*] Stephen J. Blundell [1,†] Sebastian Biesenkamp [3] Markus Braden [3,‡] Thomas C. Hansen [4] Kacper Koteras [5] Wojciech Grochala [5,§] Paolo Barone [6] José Lorenzana [7,¶] Zoran Mazej [8] and Gašper Tavčar [8]

[1]*University of Oxford, Department of Physics, Parks Road, Oxford OX1 3PU, United Kingdom*

[2]*ISIS Neutron and Muon Source, STFC Rutherford Appleton Laboratory, Chilton, Didcot OX11 0QX, United Kingdom*

[3]*II. Physikalisches Institut, Universität zu Köln, Zülpicher Straße 77, D-50937 Köln, Germany*

[4]*Institut Laue-Langevin, 71 avenue des Martyrs, CS 20156, 38042 Grenoble Cedex 9, France*

[5]*University of Warsaw, Center of New Technologies, Żwirki i Wigury 93, 02-089 Warsaw, Poland*

[6]*Superconducting and Other Innovative Materials and Devices Institute (SPIN), Consiglio Nazionale delle Ricerche, Area della Ricerca di Tor Vergata, Via del Fosso del Cavaliere 100, I-00133 Rome, Italy*

[7]*Institute for Complex Systems (ISC), Consiglio Nazionale delle Ricerche, Dipartimento di Fisica, Università di Roma "La Sapienza", 00185 Rome, Italy*

[8]*Jožef Stefan Institute, Department of Inorganic Chemistry and Technology, Jamova cesta 39, 1000 Ljubljana, Slovenia*

(Received 11 January 2023; accepted 30 March 2023; published 20 April 2023)

$KAgF_3$ is a quasi-one-dimensional quantum antiferromagnet hosting a series of intriguing structural and magnetic transitions. Here we use powder neutron diffraction, μSR spectroscopy, and density functional theory calculations to elucidate the low-temperature magnetic phases. Below $T_{N1} = 29$ K we find that the material orders as an A-type antiferromagnet with an ordered moment of $0.52\mu_B$. Both neutrons and muons provide evidence for an intermediate phase at temperatures $T_{N1} < T < T_{N2}$ with $T_{N2} \approx 66$ K from a previous magnetometry study. However, the evidence is at the limit of detection and its nature remains an open problem.

DOI: 10.1103/PhysRevB.107.144422

I. INTRODUCTION

Spin-1/2 systems show a profusion of fascinating phenomena due to strong quantum fluctuations, as the quantum effects in many-body systems increase when the mass and angular momentum of their constituents decrease. For example, light He remains liquid at zero temperature due to quantum fluctuations. By analogy, Anderson [1] proposed that spin-1/2 systems may form spin-liquid states at low temperatures, which lack long-range magnetic order. While at high dimension, the existence of spin-liquids is controversial [2], they certainly form in quasi-one-dimensional magnetic systems [3,4]. The elementary excitations called spinons have been observed with a variety of probes [5–10]. Spinons behave as fermions and can be visualized as domain walls of the local antiferromagnetic order. Although physical realizations of spin-1/2 systems are good correlated insulators, they can conduct heat as one-dimensional metals due to the fermionic properties of spinons [11]. Additionally, due to the fermionic nature of excitations, spin-1/2 systems may support a spin-Peierls instability [12], the magnetic analog of the Peierls instability in the one-dimensional electron gas.

Spin-1/2 realizations in condensed matter are represented mostly by Ti(III) or V(IV) compounds with the d^1 electronic configuration of the metal cation, and by Cu(II) systems with a d^9 electron configuration. The great diversity of the Cu(II) systems has been described in the literature with remarkable properties. For example, two-dimensional layered systems include the celebrated parent compounds [13] of high-T_c superconductors. Their strong quantum fluctuations (unlike higher-spin systems) have been recently exposed in resonant inelastic x-ray scattering studies (RIXS) [14,15]. $CuGeO_3$ is a nice example of an inorganic spin-Peierls system with a structural transition clearly linked to the magnetism [16,17]. Sr_2CuO_3 is an almost perfect realization of the one-dimensional Heisenberg model, showing an excellent example of spinon spectra in optical properties [5,6] and multispinon excitations in RIXS [7]. A gigantic spinon mean-free path has also been deduced from thermal transport [11]. CuO is a quasi-one-dimensional spin-1/2 system with much lower symmetry than Sr_2CuO_3. On lowering the temperature, it enters first into an incommensurate magnetic spiral phase and then into a commensurate antiferromagnetic phase. The incommensurate phase is also multiferroic [18]. The rich phenomenology of CuO can be understood from the intrinsic frustration built into the structure [19,20].

The analogous heavier Ag(II) congeners are much less researched [21] but their similarities to cuprates [22–24] call for an exploration of this family searching for analogous rich physics. $KAgF_3$ is one of such systems which shows intriguing structural and magnetic phenomena [25].

*john.wilkinson@stfc.ac.uk
†stephen.blundell@physics.ox.ac.uk
‡braden@ph2.uni-koeln.de
§w.grochala@cent.uw.edu.pl
¶jose.lorenzana@cnr.it

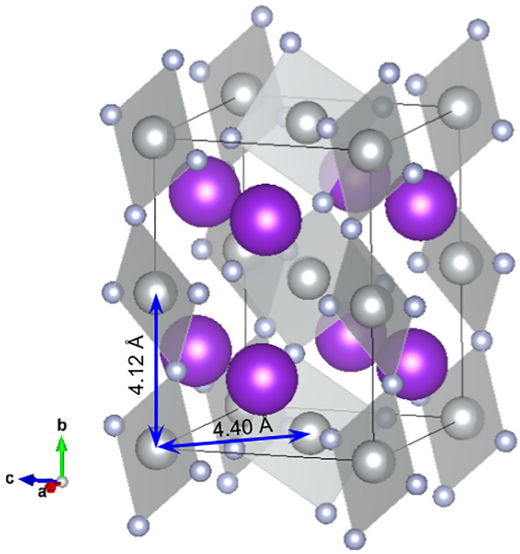

FIG. 1. Structure of $KAgF_3$. Spheres represent (in decreasing size order) K, Ag, and F. Gray plaquettes highlight short Ag-F bonds. Thin black lines indicate the orthorhombic unit cell.

This compound crystallizes in an orthorhombic unit cell (Fig. 1) which may be viewed as a distorted cubic perovskite structure. Silver-silver distances are significantly shorter along the *b* axis, as indicated in the figure. The gray plaquettes indicate short Ag-F bonds of elongated AgF_6 octahedra, with the long axis approximately perpendicular to the plaquette. The short Ag-Ag bond (4.12 Å) along the *b* axis defines kinked chains which host very strong antiferromagnetic superexchange with the coupling constant of the order of ≈100 meV from susceptibility measurements [25] or even larger according to density functional theory (DFT) computations (see Refs. [26–28] and the Supplemental Material [29]). Simultaneously, the interchain interactions are much weaker and of the order of a few meV. One can visualize the plaquettes as hosting Ag orbitals with approximately $d_{x^2-y^2}$ symmetry, with lobes pointing toward the fluorines. These mix with *p* orbitals in F along the chain, providing a robust path for superexchange [22] as in AgF_2.

A previous study [25] documented a structural transition near $T = 235$ K, accompanied by an intriguing drop of the susceptibility on lowering the temperature, which is reminiscent of a spin-Peierls transition. Magnetic order appears at lower temperatures with two magnetic transitions at $T_{N2} = 66$ K and $T_{N1} = 35$ K, whose nature has not been explored in depth so far. DFT studies suggest predominant antiferromagnetic interactions [25,28]; thus we tentatively identify T_{N1} and T_{N2} as Néel temperatures using the notation that is common in CuO.

The present work aims at elucidating the low-temperature magnetic phases of $KAgF_3$ using μSR spectroscopy, powder neutron diffraction, and density functional theory calculations [29]. Neutron scattering experiments were performed at ILL, and μSR experiments were performed at ISIS and PSI. The continuous muon source at PSI is particularly suited for detailed measurements of the magnetic ordering, while the pulsed muon source at ISIS is better for measuring details of the entanglement between the muon and the fluorine nuclei to obtain details of the muon site.

II. SAMPLE PREPARATION

A. Synthesis

Previous syntheses of $KAgF_3$ have utilized either a direct synthesis from KF and AgF_2 at elevated temperature, or a controlled thermal decomposition of a corresponding Ag(III) salt, $KAgF_4$ [25]. The latter route is quite impractical for synthesis of a large specimen (10–20 g) which is needed for neutron studies. Therefore, we followed the former procedure while using diverse Ag precursors [AgF_2, $AgNO_3$, or $KAg(CN)_2$]. A total of eleven samples were prepared. A typical procedure consisted of firing of a well-ground mixture of KF and AgF_2 (usually with small molar excess of 1.05–1.15) in a nickel container (sometimes equipped with a teflon insert) at 300 °C for 9–10 days (with small excess of F_2 gas or just with argon), followed by spontaneous cooling. The purity of each specimen was scrutinized using powder x-ray diffraction utilizing a laboratory x-ray source. The samples which proved to contain some unreacted AgF_2 or K_2AgF_4 layered perovskite (which both order ferromagnetically) were discarded. Only the five samples which were crystallographically pure or which contained no more than 1% of diamagnetic AgF were selected for further studies. All these batches were mixed together and homogenized in a prefluorinated agate mortar.

B. Sample operations

Due to the exceptionally high reactivity of Ag(II) fluorides [21], the sample selected for neutron diffraction studies was placed inside a sealed vanadium container only shortly prior to measurements. Dry ice was used to cool the sample during its transportation, and the container was kept permanently in liquid nitrogen in ILL. Similarly, a small fraction of the sample (about 0.5–1 g) from the same batch was filled into a copper container equipped with a gold O ring, and this container was immediately chilled and transported to the relevant muon facility, where it was handled inside an argon-filled glove box.

III. POWDER NEUTRON DIFFRACTION

We performed powder neutron diffraction studies on $KAgF_3$ to determine the magnetic structure on the powder diffractometer D20 at the Institut Laue-Langevin in Grenoble. We choose a large wavelength of 2.42 Å and optimized the instrument for higher flux to focus on magnetic superstructure reflections. Data were taken by scanning the entire detector unit with 1536 segments by 61 steps of 0.05° in the scattering angle 2θ. Intensities were merged into single intensity versus 2θ data normalized to a counting time of about 120 seconds. Therefore, the intrinsic statistics are much higher than the square root of the given counts. Due to the expected small moment of Ag^{2+} rather long counting was needed (in total about 4 h at 2 K and 2 h at 40 and 70 K) and indeed the observed magnetic Bragg peaks exhibit an intensity of only 0.4% compared to the strongest nuclear Bragg peak. Data sets were collected at 70 K ($>T_{N1}, T_{N2}$), 40 K (between T_{N1} and T_{N2}), and 2 K ($<T_{N1}, T_{N2}$) to cover the two magnetic

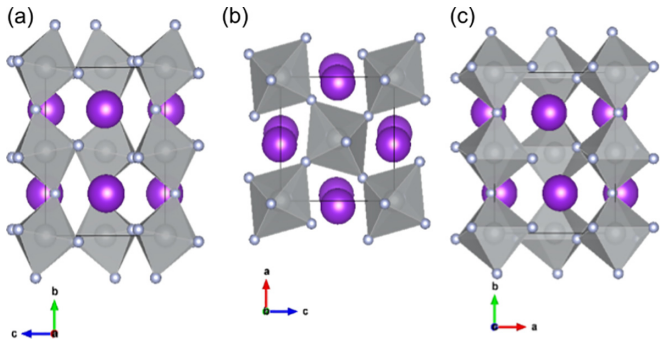

FIG. 2. Panels (a), (b), and (c) show projections of the structure along the crystallographic axis (a, b, and c, respectively) showing octahedral rotations. Thin black lines indicate the orthorhombic unit cell.

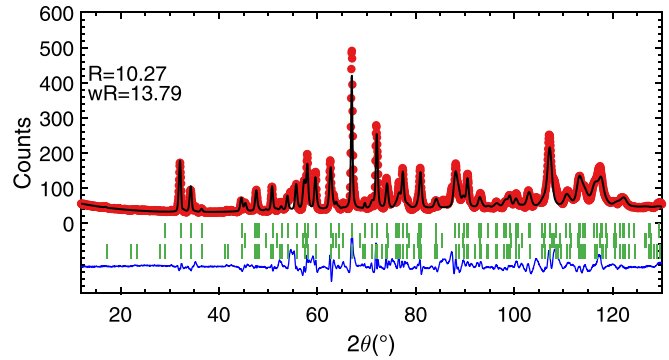

FIG. 3. Rietveld description of the data obtained on the D20 diffractometer at 2 K. Red symbols denote measured intensities, black dots the calculated ones, the blue line the differences, and vertical bars indicate the positions of Bragg reflections of the *Pnma* $KAgF_3$ and AgF_2 phases and of the $KAgF_3$ magnetic phase.

transitions deduced from magnetization studies [25]. Data are available at Ref. [30] and refinements of magnetic and nuclear structure models were performed with the FullProf program suite [31].

Previous powder x-ray diffraction studies on $KAgF_3$ observed a distorted perovskite structure, which is described with space group *Pnma* [25,32]. Distortions with this symmetry are very common in perovskites [33] and correspond to a rotation of the octahedron around the orthorhombic b axis [Fig. 2(b)], combined with tilting around nearly a which is parallel to an octahedron edge [Fig. 2(a)]. In addition, there is an elongation of the octahedra along one of the bonds in the a, c plane. This elongation rotates for neighboring sites in an a, c layer. For example, the long bonds are oriented approximately along [101] in Fig. 2(b), for the four octahedra in the corners, and nearly along $[10\bar{1}]$ for the octahedron in the center. Notice that due to the antiphase rotation of the octahedra all elongations approach the a axis forming an angle of 34° with it.

The elongation of octahedra in $KAgF_3$ can be rationalized as originating in the Jahn-Teller distortion in the d^9 configuration and indicates an orbital order with holes alternatingly occupying $x^2 - y^2$ and $z^2 - y^2$ orbitals corresponding to the staggered pattern of plaquettes in Fig. 1 (notice that here long Ag-F bonds have not been drawn). This orbital ordering determines [28] the magnetic interactions as mentioned in the Introduction.

The D20 data taken at 2 K can be well described with such a structure model, as shown in Fig. 3. We apply a correction for microscopic strain and include a small impurity AgF_2 phase, about 6% volume fraction. The refined lattice parameters are $a = 6.4106(6)$ Å, $b = 8.2597(7)$ Å, and $c = 6.0609(6)$ Å, and atomic positions are Ag at [0,0,0], K at [0.043(2),0.25,0.483(2)], F1 at [0.479(2),0.25,0.5827(13)], and F2 at [0.3159(8),0.4630(7),0.2291(12)].

The main goal of the high-flux experiments at the D20 diffractometer was to determine the magnetic structure. We searched for magnetic Bragg reflections appearing below the Néel temperatures identified by the magnetization measurements. The three diffraction patterns shown in Fig. 4 exhibit very few differences, indicating that the crystal structure does not significantly change below 70 K. For most Bragg reflections and for the background the patterns perfectly superpose; see Fig. 4(a).

Due to the high statistics and the excellent reproducibility of the diffraction experiments, we are able to analyze the tiny changes in the diffraction patterns. In the pattern at 2 K one finds an extra peak emerging at 16.9°, which exhibits an intensity of 4×10^{-3} compared to the strongest nuclear Bragg peaks. This intensity can be exactly indexed as (0,1,0) in the *Pnma* lattice, which is extinct in this space group. This reflection can be explained by an A-type magnetic order with ferromagnetic a, c layers antiferromagnetically stacked along b. Such a magnetic structure is expected for the antiferromagnetic orbital ordering described above [25,28]. Within an a, c layer, the perpendicular orbital arrangement with alternating

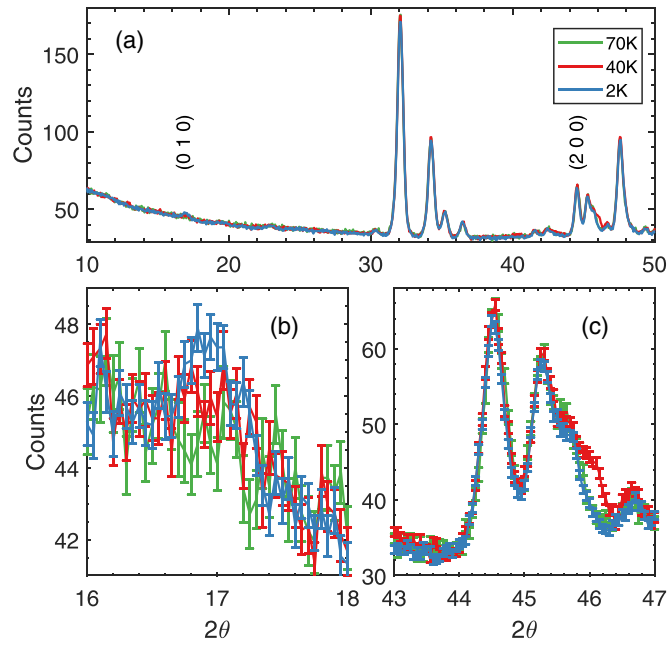

FIG. 4. Powder neutron diffraction data obtained on D20 at various temperatures focusing on the lower scattering angles (a); panels (b) and (c) present the evidence for magnetic Bragg peaks appearing in the low-temperature and intermediate magnetic phases. For clarity error bars of the intensities are given only in the lower panels.

occupation of the $x^2 - y^2$ and $z^2 - y^2$ orbitals (hole picture) implies a ferromagnetic interaction that, however, should be weak. The strongest magnetic interaction is expected for the parallel orbital arrangement along b due to strong hybridization. This orbital and magnetic arrangement was already proposed by Zhang *et al.* [28]. Since we observe the (0,1,0) Bragg reflection as the main magnetic Bragg peak the ordered moment must point perpendicular to b which is consistent with our DFT computations (see the Supplemental Material [29]) and with the muon results to be shown below. The refinement of magnetic models cannot distinguish between alignment along the a or c direction, but the symmetry analysis with representation theory indicates that an A-type order with moments along the a direction permits the occurrence of a weak ferromagnetic moment along b, which is not seen in the magnetization data [25]. Therefore, only the A-type order with moments along c is possible. The model yields an ordered moment of $\mu_{Ag} = 0.47(15)\ \mu_B$ assuming the Pd^{1+} form factor [34] and allows for a canting of moments with G-type x and C-type y components. For the 4d Ag moment one may expect sizable canting but its determination is well beyond the precision of our experiment. This value of the magnetic moment agrees well with the moment determined by the μSR experiments (as reported in the next section) when assuming a c orientation, while for an a orientation the muon analysis yields a much smaller moment. This gives further support to the conclusion that the main A-type component of the magnetic moment in $KAgF_3$ is parallel to c.

The (0,1,0) magnetic intensity is absent at 40 K [see Fig. 4(b)] consistent with the lower magnetic transition observed in the susceptibility at $T_{N1} \approx 35$ K [25]. In the data at 40 K however, there is extra intensity at 46° that is not visible either in the 2 K or in the 70 K data. Note that the higher magnetic transition is found at 66 K in the magnetization. This intensity can be indexed as (1.3,1,1.3) but with the single magnetic reflection the magnetic structure cannot be determined. Possibly this magnetic structure not only differs in the propagation vector but also in the direction of the ordered moment. A tempting possibility would be a spiral, possibly commensurate magnetic structure at $(1/3, 0, 1/3)$. Notice that in this case, the canting of adjacent moments would occur along small-J bonds. Indeed, our DFT computations lead to a very small cost of the spiral (see the Supplemental Material [29]). Thus, it is plausible that the small energetic penalty of forming the spiral is overcome by entropic effects. Such intermediate spiral phases are common in frustrated systems, for example in the multiferroic phase of CuO [18–20]. Here, such a possibility would make $KAgF_3$ an analog of CuO, perhaps with multiferroic properties.

In the next section, we will report on the magnetic phases from the point of view of μSR spectroscopy. This will provide further information on the magnetic phases. The μSR experiment, however, does not find evidence for magnetic order at this temperature range. This discrepancy requires further analysis.

IV. μSR RESULTS AND ANALYSIS

μSR spectroscopy is an excellent technique to detect local magnetic environments: in this technique, positive muons are implanted in the sample, and stop somewhere in the crystal [35]. Hence, muons act as local magnetometers, so for a fully quantitative analysis of μSR data it is important to determine the stopping site. To this aim we have performed *ab initio* DFT+μ calculations [36,37], which we report now.

TABLE I. DFT+μ results, showing the energies above the lowest energy site.

Site	Position (fractional coordinates)	Energy (meV)
1	(0.7934, 0.4950, 0.5802)	0
2	(0.6829, 0.3203, 0.4336)	123

A. Muon site calculations

The DFT+μ calculations resulted in two feasible sites, which are shown in Table I, with all other sites discounted due to having an energy far above these [29]. These two candidate muon sites are depicted in Fig. 5(a). As is usually the case for muons implanting in fluoride samples, DFT+μ predicts that the muon will draw in the two nearest fluorines toward it for both sites. Although DFT often struggles to calculate the extent of these distortions to a high accuracy, we estimate that for site 1 the nearest-neighbor fluorine goes from being 1.35 Å from the muon to 1.09 Å, and for site 2 the nearest-neighbor moves from 1.82 Å to 1.05 Å, and we expect these bond-length estimates to be correct to within 0.1–0.2 Å. These large lattice distortions have been observed in other fluorides and are attributed to the formation of so called "strong" hydrogen-like bonds [38–41] analogous to the ones in HF_2^- ions [42]. Figure 5(b) shows the extent of these lattice distortions in site 2 (site 1 has similar distortions, but this site is inconsistent with the data, which we will discuss later).

B. $T < T_{N1}$: Measuring the collinear magnetic order

The sample was contained in a Cu sample holder and placed in the GPS spectrometer at PSI. Data from this experiment are shown in Fig. 6(a), and show a clear oscillatory

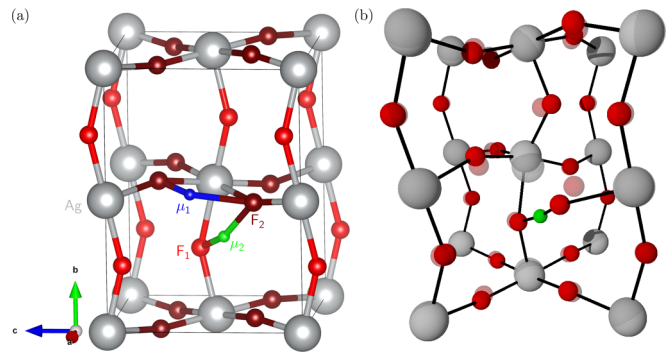

FIG. 5. $KAgF_3$ muon sites. (a) shows the two candidate muon sites as described in Table I, and (b) shows site 2 with its undistorted and distorted atoms in its unit cell as translucent and opaque spheres, respectively. The two Wyckoff sites occupied by fluorine atoms are denoted as F_1 and F_2, and are drawn as different shades of red.

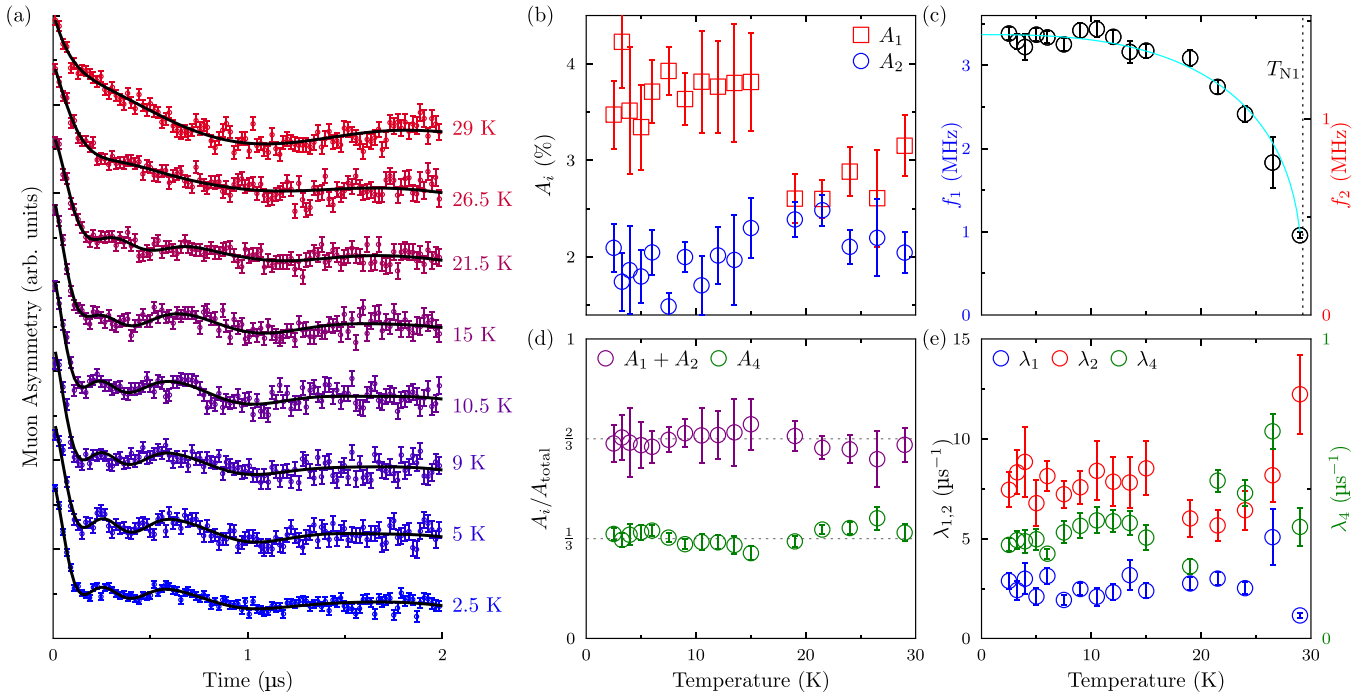

FIG. 6. (a) shows the short-time μSR data with the sample holder background removed, where the oscillations can be clearly observed. The black lines represent the fit to Eq. (3), as described in the text. (b) shows how the amplitudes of the two oscillating components A_1 and A_2 vary with temperature, and (c) shows the frequency of these oscillations (the cyan line shows the fit to the model as described in the text). (d) shows how the relative amplitude of the two varying oscillating components (A_1 and A_2) and the nonoscillating component A_4 vary with temperature, and (e) shows the relaxation rate of these components.

feature at short timescales which is very heavily damped, and this remains present up to around 31 K. Above 31 K, no oscillations due to magnetic ordering were observed in the muon asymmetry. Some muons were found to stop in the Cu sample holder, which creates a Kubo-Toyabe component in the muon asymmetry [43,44], which we modeled using the dynamic Gaussian Kubo-Toyabe polarization function $G_{\mathrm{DKT}}(t)$, given by

$$G_{\mathrm{DKT}}(t) = g(t)e^{-\nu t} + \nu \int_0^t g(\tau)e^{-\nu\tau} G_{\mathrm{DKT}}(t-\tau)d\tau, \quad (1)$$

with

$$g(t) = \frac{1}{3} + \frac{2}{3}(1-\Delta^2 t^2)\exp\left(-\frac{\Delta^2 t^2}{2}\right). \quad (2)$$

Here, Δ is the standard deviation of the internal fields at the muon site in the copper, which was fount to be constant across the temperature range studied and was therefore fixed to $\Delta = 0.34(1)$ μs^{-1}. Earlier work by Kadono *et al.* shows that the dynamical hop rate ν varies considerably in this temperature region, and since we had insufficient decay statistics to fit this we used the values reported in Ref. [43] for each of the temperatures studied. The amplitude of this background function in the muon asymmetry was constant at 8.81(21)%, and this function was subtracted from the data for the subsequent analysis [29].

The data, with the copper background subtracted, were fitted with the function

$$A(t) = \sum_{i=1}^{3} A_i \cos(2\pi f_i t - \phi_i)e^{-\lambda_i t} + A_4 e^{-\lambda_4 t}, \quad (3)$$

for $t \in [0, 2]\mu_s$, where each oscillating component usually represents muons stopped in different sites in the sample, precessing in their local magnetic fields ($B_i = 2\pi f_i/\gamma_\mu$, with $\gamma_\mu = 2\pi \times 135.5$ MHz T^{-1}), with a relaxation $e^{-\lambda_i t}$ due to field fluctuations caused by spin dynamics and inhomogeneities [35]. The term $A_4 e^{-\lambda_4 t}$ models muons stopping in a site where their initial spin polarization is parallel to the local magnetic field and hence the muon polarization decays due to the aforementioned decay processes without undergoing precession. Many of these fitting parameters were found to be constant throughout the range of the temperatures studied. Therefore, they were fixed to the following values: $\phi_1 = 0(10)^\circ$, $\phi_2 = 0.0(1)^\circ$, $A_3 = 0.49(10)\%$, $\phi_3 = -44(25)^\circ$, $f_3 = 0.62(9)$ MHz, and $\lambda_3 = 0.22(17)$ μs^{-1}. After initially being allowed to vary, it was found that the ratio between the frequencies f_1 and f_2 was constant at $1 : 0.424(1)$, and was also fixed for the subsequent analysis.

The values of the parameters which were allowed to vary are plotted in Figs. 6(b)–6(e). In particular, A_1 and A_2 have a highly unusual temperature dependence [Fig. 6(b)], but the ratio $A_1 + A_2 : A_4$ is broadly constant at $\frac{2}{3} : \frac{1}{3}$ [Fig. 6(c)], a point we will return to in Sec. IV D. As the frequencies of A_1 and A_2 clearly show order-parameter-like behavior, and the relaxation of these components and A_4 show a divergence

around the critical temperature T_{N1}, we can attribute these components to muons stopping in the $KAgF_3$ sample. As the A_3 term exhibits no order-parameter-like behavior, it can be assumed to be due to a muon stopping in an impurity in the sample, the frequency of which is consistent with precession in a very small magnetic field, or indeed it may be due to the muon becoming entangled with fluoride impurities leading to very low amplitude F-μ-F oscillations (see the Supplemental Material for a discussion of these states [29]).

The f_1 values were fitted to the phenomenological fitting function

$$f(T) = f_0\left(1 - \left(\frac{T}{T_{N1}}\right)^{\alpha}\right)^{\beta}, \tag{4}$$

to model the critical behavior of the low-temperature phase. The fitting parameters obtained were $T_{N1} = 29.26(3)$ K, $f_0 = 3.37(3)$ MHz, $\alpha = 2.7(3)$, and $\beta = 0.338(7)$. The critical temperature T_{N1} is slightly lower than the 35 K measured by magnetic susceptibility [25], but this is consistent with what was measured at ISIS (see next section and the Supplemental Material [29]). The value of β characterizes the critical behavior of the sample, and is consistent with the value one would expect from a 3D Ising-like system (which predicts $\beta = 0.326$), though the number of data points in the critical regime is very low and so this should only be taken as a crude estimate. This result suggests an easy-axis anisotropy, which is indeed confirmed by the DFT computations reported below.

C. $T > T_{N1}$: Muon-fluorine entangled states

The sample was also placed in the MuSR spectrometer at the STFC-ISIS muon facility, Rutherford Appleton Laboratory, UK. Below the transition temperature, it was possible to observe characteristic signs of magnetic ordering, but it was not possible to resolve these with the time resolution of the spectrometer (the ISIS data for $T < T_{N1}$ are shown in the Supplemental Material [29]). Above the transition temperature, the characteristic oscillations expected from muon-fluorine entanglement were observed [38–41].

Therefore, the muon asymmetry data for temperatures above T_{N1} were fitted to the function

$$A(t) = A_r P_{F\mu F}(r_{nn1}, r_{nn2}, r_{\mu Ag}; t) + A_{Cu} G_{DKT}(\Delta, \nu; t) + A_{bg}, \tag{5}$$

where the first term represents muons stopped in the $KAgF_3$ crystal and evolving due to the entanglement between itself and the surrounding fluoride nuclei, which is calculated as described in the Supplemental Material [29]. This function has the fitting parameters r_{nn1} and r_{nn2} to represent the distance from the muon to the closest and next-closest nearest-neighbor fluorides, respectively (μ_2 to the nearest F2 and F1 in Fig. 5, respectively), and $r_{\mu Ag}$ is the distance from the muon to the nearest-neighbor Ag ion. The second term represents muons stopped in the Cu sample holder [Eqs. (1) and (2), accounting for 11.9% of the total asymmetry], and the final term represents muons stopped elsewhere but not undergoing any precession or relaxation which is measurable.

We found that calculating $P_{F\mu F}(t)$ for both the sites found with DFT+μ in Table I produced a very similar result, meaning that the two muon sites were indistinguishable with the ISIS data. However, the careful analysis of the dipole fields of both sites and the comparison of this to the PSI data (as discussed in Sec. IV D) shows that the only site which is realized by the muon is site 2.

The fits to Eq. (5) are shown in Fig. 7(a) and the fitting parameters obtained are plotted in Figs. 7(b) and 7(c). Figure 7(a) demonstrates the impressive agreement between the model and the data up to 105 K (muon diffusion occurs at very high temperatures and this is outside the scope of our model). The change in A_{bg} and A_r is somewhat unusual, suggesting some sort of phase transition between 50 and 70 K, perhaps related to the susceptibility anomaly [25] at T_{N2} and giving further support for the existence of an intermediate magnetic phase. Unfortunately, there is insufficient muon data in this temperature range to be able to determine the cause of this. Yet, it is important to note that as F-μ-F states are highly suppressed by magnetic fields (since the field at the muon site due to the ordering of the electronic moments tends to be much larger than that due to the nuclear moments), this is unlikely to be due to static magnetic ordering.

The fits also show that the F-μ-F complex changes slightly with temperature, with a change in bond length of around 0.08 Å across the whole temperature range. This is likely to be due to the way in which the entire structure of the crystal changes with temperature, as has been reported previously [25]. The DFT+μ results show that the two nearest-neighbor fluorines are $r_{nn1}^{DFT} = 1.05$ Å and $r_{nn2}^{DFT} = 1.30$ Å, which are close to the values measured here. Additionally, the μ-Ag distance $r_{\mu Ag}$ varied very little with temperature, and was found to be 2.34(6) Å, very close to the value of 2.35 Å calculated with DFT.

D. Calculation of the Ag magnetic moment with μSR

A muon implanted in a sample precessses in its local magnetic field due to the Zeeman interaction. Assuming that the only origin of this field in $KAgF_3$ is due to the dipolar field of the surrounding magnetic moments B_{dip}, the local field of the muon can be calculated as

$$\mathbf{B}_{dip} = \sum_i \frac{\mu_0}{4\pi r_i^3}[3(\boldsymbol{\mu}_i \cdot \hat{\mathbf{r}}_i)\hat{\mathbf{r}}_i - \boldsymbol{\mu}_i], \tag{6}$$

where the sum is over the surrounding Ag ions with a magnetic moment $\boldsymbol{\mu}_i$ at a distance r_i from the muon. This sum is taken over a large Lorentz sphere of radius 150 Å, and as the material is antiferromagnetic the lack of bulk magnetization means no additional term is required to account for moments beyond this.

One can then use Eq. (6) to calculate the dipole fields at both the muon sites predicted by DFT, assuming ferromagnetically ordered moments in the a, c plane and antiferromagnetic along b, with all moments constrained to point in the c direction, as predicted by our DFT calculations of the magnetic structure reported in the Supplemental Material [29]. From this, assuming the moment of the Ag ions $\mu_{Ag} = 0.55\mu_B$, the field at the muon site would be 643 G for site 1, and 260 G for site 2, leading to muon precession frequencies of around 8.7 MHz and 3.5 MHz, respectively. In accord with the analysis of Sec. IV B, the precession frequency of site 2

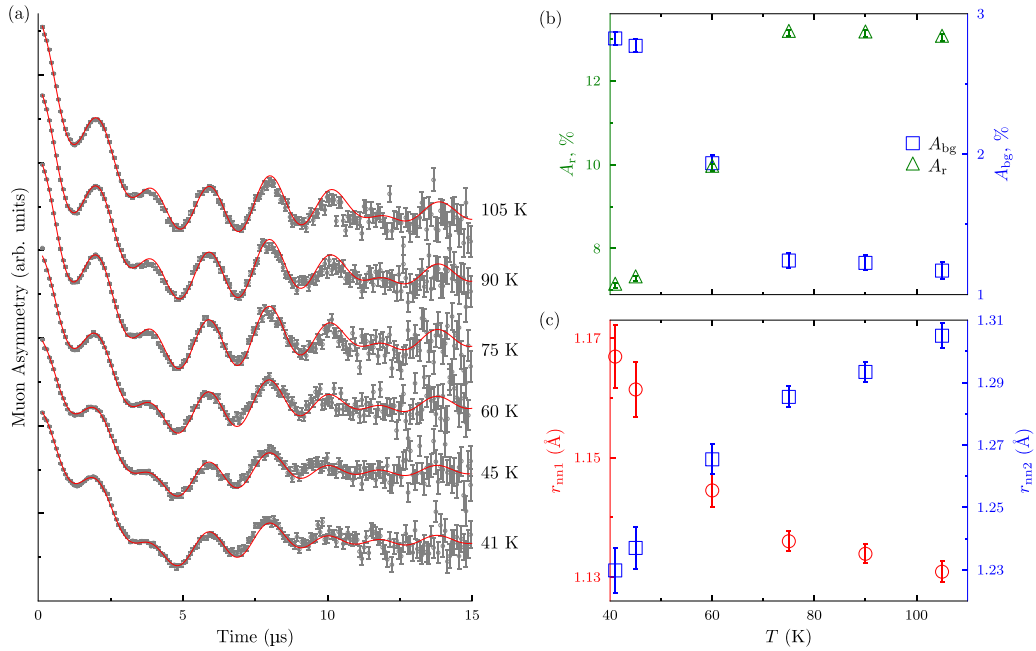

FIG. 7. Fits to the ISIS data. (a) shows the fits to the data using the model described in the text. (b) shows the variation of the relaxing asymmetry A_r and background asymmetry A_{bg} with temperature T, and (c) shows how the μ-F distances r_{nn1} and r_{nn2} vary.

is significantly closer to that measured, and therefore we will assume that this is the correct muon site for the rest of the analysis. As the distance between the muon and the nearest Ag ion was found to be 2.33(6) Å by fitting the ISIS data, the moment on the Ag ion can be determined. Again using the dipole field calculations, the moment on the Ag ions is calculated as $\mu_{Ag} = 0.517(4)\mu_B$, in excellent agreement with the value determined with neutrons (Sec. III) and only slightly smaller than the value of $0.549\mu_B$ predicted by our DFT results (see the Supplemental Material [29]). Such an overestimation is not surprising, as is common [45,46] to other mean-field-like approaches that neglect transverse quantum fluctuations.

Other valid potential magnetic structures for this compound have the moments aligned along the a direction, and in any other direction along the a, c plane. If the spins are aligned along a, following the same calculation as above results in an Ag electronic moment of $0.207(2)\mu_B$, which is significantly smaller than the moment calculated both from the neutron data and by the DFT calculations, and is therefore an unlikely magnetic structure. If the moments are aligned along an intermediate direction in the a, c plane, one would expect the muon data to have two frequencies with an equal magnitude (owing to the site symmetry), which is not realized in the data (although it is important to note that the measured muon precession at this frequency relaxes very quickly, so moments pointing in an intermediate direction cannot conclusively be ruled out).

E. Origin of the two frequencies in the PSI data

As discussed in Sec. IV B, the PSI data show two oscillations with frequencies f_1 and f_2 which follow the same order parameter. The two frequencies could be associated with two distinct muon sites, as was proposed in related studies of $KCuF_3$ and Cs_2AgF_4 [47,48], but the temperature-dependent nature of the amplitudes A_1 and A_2 shown in Fig. 6(b), together with the single site assumed for fitting the F-μ-F oscillations [which works so well, as shown in Fig. 7(a)], points instead to a different interpretation. We propose that the origin of the second oscillation is due to the effect of the nearest-neighbor fluorine nucleus precessing in its own local magnetic field resulting from the ordered Ag^{2+} electronic moments, which then affects the state of the muon. One can picture this by considering both the muon and fluorine to be classical dipoles in a magnetic field. Before the muon implantation, the fluorine nuclear spin is in a fully mixed state. But once the polarized muon is implanted and the lattice distorted, the fluorine becomes slightly polarized by the muon, and the field at the fluorine is modified due to the strong lattice distortion. Hence, the fluorine and muon *both* undergo Larmor precession in the field produced by the ordered Ag^{2+} moments, but the dipole-dipole interaction between them creates a field at the muon site that depends on the orientation of the nuclear spin of the fluorine with respect to the local field direction at the fluorine site. The field at the nearest-neighbor fluorine site (assuming the magnetic structure of $KAgF_3$ described above) is calculated as 347 G, which is larger than that of the muon (235 G), and points in a different direction.

In order to model the two frequencies, one can calculate the expected amplitudes and frequencies of the muon polarization using the Hamiltonian in the Supplemental Material [29], for the case of a system with a muon and one fluorine (the other fluorine is further away, so it does not have such a large effect). This produces the precession frequencies (for a large magnetic field) of

$$\omega_\mu^\pm = \gamma_\mu B_\mu \pm \delta_\mu,$$
$$\omega_F^\pm = \gamma_F B_F \pm \delta_F,$$
$$\omega_F \pm \omega_\mu = \gamma_F B_F \pm \gamma_\mu B_\mu,$$

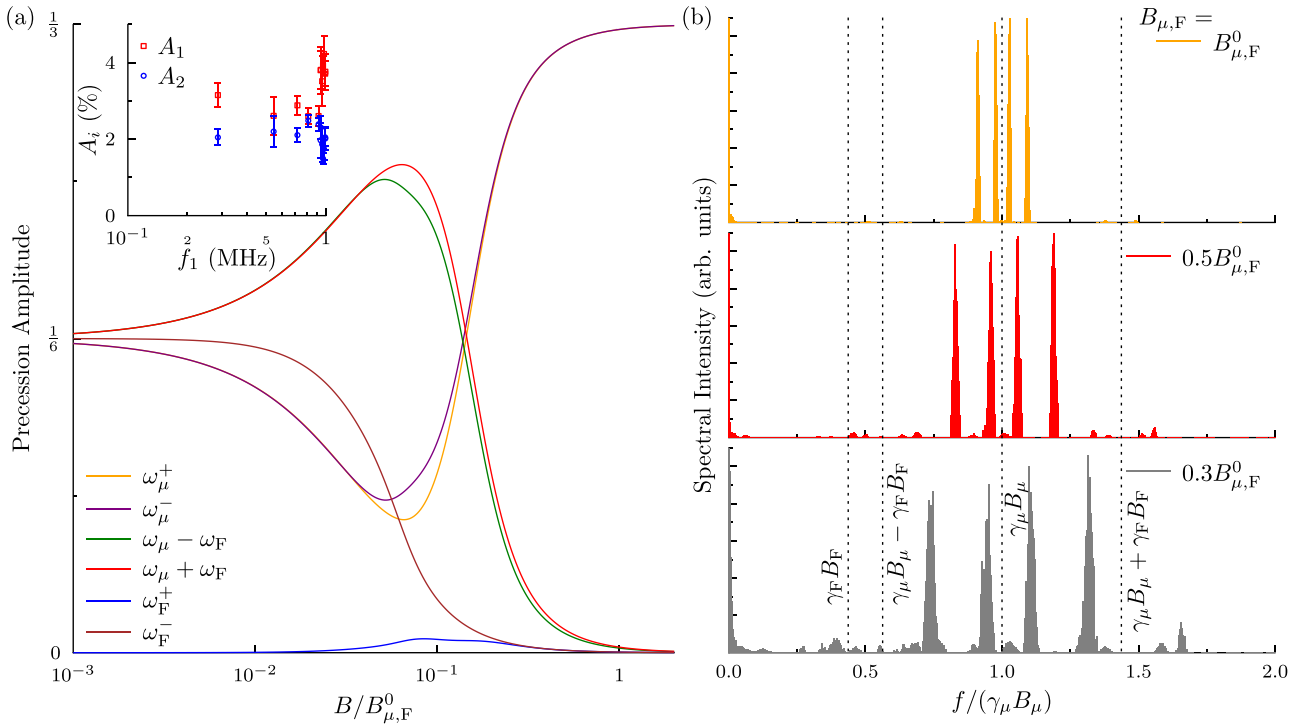

FIG. 8. F-μ states in a magnetic field. (a) shows how the amplitudes of the components of the muon precession signal vary as the field on the muon and fluorine sites is scaled by a factor $B/B^0_{\mu,\mathrm{F}}$ (the key shows the value of these precession frequencies as $B \to \infty$). The inset shows how the amplitudes A_1 and A_2 of the two measured components vary with the muon precession frequency, showing how at low fields A_1 and A_2 become closer in value, in support of this model. (b) shows the Fourier transform of the system of the muon coupled to its nearest- and next-nearest-neighbor spins, for the field at the muon and fluorine sites scaled by various amounts, as shown in the legend for each of the subplots.

where δ_μ and δ_F are the splittings due to the dipole-dipole coupling between the muon and the fluorine, which depends on the geometry of the F-μ bond with respect to the magnetic fields, and is around $0.2003\omega_\mathrm{D}$ for this case ($\omega_\mathrm{D} = \frac{\mu_0 \gamma_\mu \gamma_\mathrm{F}}{4\pi\hbar|\mathbf{r}|^3} = 1.507$ Mrad s^{-1} from the ISIS data for this geometry). The amplitude of the signals corresponding to these states is plotted in Fig. 8(a), for the field at the muon and fluorine sites, scaled by various amounts. This shows that, when the fields at the muon and fluorine sites are very large, the only precession frequencies observable are due to the muon precessing at its Larmor frequency. However, for the relatively small fields seen in $KAgF_3$, the figure shows that the $\omega_\mathrm{F}^\pm$ and $\omega_\mathrm{F} \pm \omega_\mu$ terms increase as the magnetic fields decrease, which occurs when the temperature approaches the transition.

The inset to Fig. 8(a) shows how the amplitudes of the two components A_1 and A_2 vary with the precession frequency f_1. This shows a clear trend of A_1 decreasing as A_2 increases, which is consistent with this model, despite the effect being more pronounced in the data as one would expect from the theory. Expanding this model to consider also the next-nearest-neighbor interactions, the amplitudes of these oscillations change slightly, as shown in Fig. 8(b). This shows the Fourier components of the expected muon polarization, showing peaks close to many of the frequencies of the F-μ case (but many of these are broadened out by the next-nearest-neighbor dipole-dipole interactions making them very small). Decreasing the field further, it can be seen that the peaks just below around 50% of the muon Larmor frequency start to emerge, which is broadly consistent with the $f_1 : f_2$ ratio found previously. We therefore tentatively assign the component with amplitude A_2 to this cluster of frequencies [which correspond to $\omega_\mathrm{F}^\pm$ in Fig. 8(a)].

V. CONCLUSIONS

The combined powder neutron diffraction and muon spin rotation studies as well as theoretical DFT calculations on $KAgF_3$ allowed us to unequivocally determine the magnetic ground state of this compound as an ordered A-type antiferromagnet with a Néel temperature $T_{\mathrm{N1}} = 29$ K. This is close to the temperature of 35 K, where an anomaly was found in the susceptibility data [25]. In Ref. [25], another anomaly was reported at $T_{\mathrm{N2}} \approx 66$ K, so it is natural to ask if there is an intermediate magnetically ordered phase between T_{N1} and T_{N2}. Neutron diffraction experiments provide evidence for an incommensurate phase in this temperature region; however the signal is rather weak and insufficient to determine the magnetic structure. A strong temperature dependence of a background contribution in the analysis of the muon data suggests some kind of phase transition in the same temperature range. On the other hand, there is no evidence of static moments, even with an incommensurate arrangement, as would be suggested by the neutrons. Therefore, the possibility of an intermediate magnetic phase between the ground state and the disordered paramagnet, analogous to CuO [18], remains

TABLE II. The Néel point, intrachain and interchain magnetic superexchange constants (in units of kelvins), reduced Néel temperature, and magnetic anisotropy for $KCuF_3$ and $KAgF_3$. Experimental values of Néel temperature and exchange constants for $KAgF_3$ are from Ref. [25]. For $KCuF_3$, values are from Ref. [49] and references therein.

Compound	T_N	J_{1D}	J_{perp}	T_N/J_{1D}	$-J_{perp}/J_{1D}$
$KCuF_3$	39	406	−21	9.6×10^{-2}	5.2×10^{-2}
$KAgF_3$	29.3	1160	−13.5	2.5×10^{-2}	1.2×10^{-2}

an open problem. Another interesting open problem is the origin of the structural transitions near $T = 235$ K and the relationship between this with the magnetic ordering, if any. A detailed structural study is under way to solve this issue.

It is interesting to compare the present results with $KCuF_3$. Following Yasuda *et al.* [50], we may now determine the value of J_{perp}, which turns out to amount to −13.5 K (as shown in Table II). From our DFT computations we estimate a value of $J_{1D} = 173$ meV (2000 K) and taking an effective $|J_{perp}| = |J_{ac} + (J_a + J_c)/2| \approx 4.25$ (50 K) meV (obtained by averaging over calculated interchain exchange interactions; see the Supplemental Material [29]) we obtain $|J_{perp}/J_{1D}| = 2.5 \times 10^{-2}$, of the same order of magnitude as the experimental one. The theoretical J_{1D} appears somewhat larger than the experimental result and previous DFT studies [25,28], probably because of details on the functional used. We notice, however, that even if we plug the calculated J_{1D} in the formula of Yasuda *et al.* [50], we get $J_{perp} = -12.8$ K, with a marginal impact on the ratio $|J_{perp}/J_{1D}| = 1.1 \times 10^{-2}$. Therefore, $KAgF_3$ seems to exhibit an approximately 4 times larger bond anisotropy in inter- and intrachain exchange interactions than its Cu analog, which is manifested in a smaller T_N value for the former, and the J_{1D} being at least 3 times larger for the Ag than for the Cu compound.

ACKNOWLEDGMENTS

Research was carried out with the use of CePT infrastructure financed by the European Union—the European Regional Development Fund within the Operational Programme "Innovative economy" for 2007–2013 (Grant No. POIG.02.02.00-14-024/08-00). The Polish authors are grateful to Narodowe Centrum Nauki (Poland) for support (Maestro, Grant No. 2017/26/A/ST5/00570). Part of this work was funded by UK Research and Innovation (UKRI) under the UK government's Horizon Europe funding guarantee [Grant No. EP/X025861/1]. The Italian authors acknowledge financial support from the Italian MIUR through Projects No. PRIN 2017Z8TS5B and No. PRIN 20207ZXT4Z. The Slovenian authors acknowledge the financial support of the Slovenian Research Agency (Research Core Funding No. P1-0045; Inorganic Chemistry and Technology). The German authors acknowledge funding by the Deutsche Forschungsgemeinschaft (DFG; German Research Foundation), Project No. 277146847, CRC 1238, Project No. B04. W.G. is grateful to the Interdisciplinary Center for Mathematical and Computational Modelling, University of Warsaw, for the availability of high performance computing resources (Okeanos, Topola) within Projects No. G29-3 and No. GA83-34. The muon data for $T < T_{N1}$ were taken at the Swiss Muon Source, PSI, Switzerland, and J.M.W. and S.J.B. would like to thank Chennan Wang for running the experiment. The muon data for $T > T_{N1}$ were taken at the ISIS Neutron and Muon Source, UK, and we would like to thank Francis Pratt for his assistance [51]. The DFT+μ calculations were done both on the Redwood cluster at the University of Oxford with the assistance of Jonathan Patterson, and also using the STFC's SCARF cluster.

[1] P. W. Anderson, Mater. Res. Bull. **8**, 153 (1973).
[2] S. Sorella, Y. Otsuka, and S. Yunoki, Sci. Rep. **2**, 992 (2012).
[3] S. E. Dutton, M. Kumar, M. Mourigal, Z. G. Soos, J.-J. Wen, C. L. Broholm, N. H. Andersen, Q. Huang, M. Zbiri, R. Toft-Petersen, and R. J. Cava, Phys. Rev. Lett. **108**, 187206 (2012).
[4] L. Savary and L. Balents, Rep. Prog. Phys. **80**, 016502 (2017).
[5] H. Suzuura, H. Yasuhara, A. Furusaki, N. Nagaosa, and Y. Tokura, Phys. Rev. Lett. **76**, 2579 (1996).
[6] J. Lorenzana and R. Eder, Phys. Rev. B **55**, R3358 (1997).
[7] J. Schlappa, U. Kumar, K. J. Zhou, S. Singh, M. Mourigal, V. N. Strocov, A. Revcolevschi, L. Patthey, H. M. Rønnow, S. Johnston, and T. Schmitt, Nat. Commun. **9**, 5394 (2018).
[8] M. Enderle, B. Fåk, H. J. Mikeska, R. K. Kremer, A. Prokofiev, and W. Assmus, Phys. Rev. Lett. **104**, 237207 (2010).
[9] B. Lake, D. A. Tennant, J. S. Caux, T. Barthel, U. Schollwöck, S. E. Nagler, and C. D. Frost, Phys. Rev. Lett. **111**, 137205 (2013).
[10] M. Mourigal, M. Enderle, A. Klöpperpieper, J. S. Caux, A. Stunault, and H. M. Rønnow, Nat. Phys. **9**, 435 (2013).
[11] C. Hess, Phys. Rep. **811**, 1 (2019).
[12] T. Giamarchi, *Quantum Physics in One Dimension*, International Series of Monographs on Physics (Oxford University Press, Oxford, 2004).
[13] M. A. Kastner, R. J. Birgeneau, G. Shirane, and Y. Endoh, Rev. Mod. Phys. **70**, 897 (1998).
[14] D. Betto, R. Fumagalli, L. Martinelli, M. Rossi, R. Piombo, K. Yoshimi, D. Di Castro, E. Di Gennaro, A. Sambri, D. Bonn, *et al.*, Phys. Rev. B **103**, L140409 (2021).
[15] L. Martinelli, D. Betto, K. Kummer, R. Arpaia, L. Braicovich, D. Di Castro, N. B. Brookes, M. Moretti Sala, and G. Ghiringhelli, Phys. Rev. X **12**, 021041 (2022).
[16] M. Hase, I. Terasaki, and K. Uchinokura, Phys. Rev. Lett. **70**, 3651 (1993).
[17] M. Braden, G. Wilkendorf, J. Lorenzana, M. Aïn, G. J. McIntyre, M. Behruzi, G. Heger, G. Dhalenne, and A. Revcolevschi, Phys. Rev. B **54**, 1105 (1996).
[18] T. Kimura, Y. Sekio, H. Nakamura, T. Siegrist, and A. P. Ramirez, Nat. Mater. **7**, 291 (2008).
[19] G. Giovannetti, S. Kumar, A. Stroppa, J. van den Brink, S. Picozzi, and J. Lorenzana, Phys. Rev. Lett. **106**, 026401 (2011).

[20] J. Hellsvik, M. Balestieri, T. Usui, A. Stroppa, A. Bergman, L. Bergqvist, D. Prabhakaran, O. Eriksson, S. Picozzi, T. Kimura, and J. Lorenzana, Phys. Rev. B **90**, 014437 (2014).

[21] W. Grochala and R. Hoffmann, Angew. Chem. Int. Ed. **40**, 2742 (2001).

[22] J. Gawraczyński, D. Kurzydłowski, R. A. Ewings, S. Bandaru, W. Gadomski, Z. Mazej, G. Ruani, I. Bergenti, T. Jaroń, A. Ozarowski, S. Hill, P. J. Leszczyński, K. Tokár, M. Derzsi, P. Barone, K. Wohlfeld, J. Lorenzana, and W. Grochala, Proc. Natl. Acad. Sci. USA **116**, 1495 (2019).

[23] N. Bachar, K. Koteras, J. Gawraczynski, W. Trzciński, J. Paszula, R. Piombo, P. Barone, Z. Mazej, G. Ghiringhelli, A. Nag, K.-j. Zhou, J. Lorenzana, D. van der Marel, and W. Grochala, Phys. Rev. Res. **4**, 023108 (2022).

[24] R. Piombo, D. Jezierski, H. P. Martins, T. Jaroń, M. N. Gastiasoro, P. Barone, K. Tokár, P. Piekarz, M. Derzsi, Z. Mazej, M. Abbate, W. Grochala, and J. Lorenzana, Phys. Rev. B **106**, 035142 (2022).

[25] D. Kurzydłowski, Z. Mazej, Z. Jagličić, Y. Filinchuke, and W. Grochala, Chem. Commun. **49**, 6262 (2013).

[26] D. Kurzydłowski and W. Grochala, Angew. Chem. Int. Ed. **56**, 10114 (2017).

[27] D. Kurzydłowski and W. Grochala, Phys. Rev. B **96**, 155140 (2017).

[28] X. Zhang, G. Zhang, T. Jia, Y. Guo, Z. Zeng, and H. Q. Lin, Phys. Lett. A **375**, 2456 (2011).

[29] See Supplemental Material at http://link.aps.org/supplemental/10.1103/PhysRevB.107.144422 for more details of the sample synthesis, x-ray analysis, density functional theory calculations, and μSR. This material also contains Refs. [25,27,28,35,40,41,52–54].

[30] W. Grochala, S. Biesenkamp, M. Braden, T. Hansen, K. Koteras, and J. Lorenzana, Spin-Peierls transitions and magnetic ordering in $KAgF_3$, Institut Laue-Langevin, doi:10.5291/ILL-DATA.5-31-2635.

[31] J. Rodríguez-Carvajal, Phys. B: Condens. Matter **192**, 55 (1993).

[32] Z. Mazej, E. Goreshnik, Z. Jagličić, B. Gaweł, W. Łasocha, D. Grzybowska, T. Jaroń, D. Kurzydłowski, P. Malinowski, W. Koźminski, J. Szydłowska, P. Leszczyński, and W. Grochala, CrystEngComm **11**, 1702 (2009).

[33] J.-S. Zhou and J. B. Goodenough, Phys. Rev. Lett. **94**, 065501 (2005).

[34] Due to the rather small Q value the form factor has little impact in this case. See the supplementary information to Ref. [22] for a comparison of the Pd_1^+ form factor and a DFT computation of Ag^{2+} form factors.

[35] S. J. Blundell, R. De Renzi, T. Lancaster, and F. L. Pratt, editors, *Introduction to Muon Spectroscopy* (Oxford University Press, Oxford, 2022).

[36] J. S. Möller, D. Ceresoli, T. Lancaster, N. Marzari, and S. J. Blundell, Phys. Rev. B **87**, 121108(R) (2013).

[37] F. Bernardini, P. Bonfà, S. Massidda, and R. De Renzi, Phys. Rev. B **87**, 115148 (2013).

[38] J. H. Brewer, S. R. Kreitzman, D. R. Noakes, E. J. Ansaldo, D. R. Harshman, and R. Keitel, Phys. Rev. B **33**, 7813 (1986).

[39] D. R. Noakes, E. J. Ansaldo, S. R. Kreitzman, and G. M. Luke, J. Phys. Chem. Solids **54**, 785 (1993).

[40] J. M. Wilkinson and S. J. Blundell, Phys. Rev. Lett. **125**, 087201 (2020).

[41] J. M. Wilkinson, F. L. Pratt, T. Lancaster, P. J. Baker, and S. J. Blundell, Phys. Rev. B **104**, L220409 (2021).

[42] B. J. Emsley and S. H. Bonds, Chem. Soc. Rev. **9**, 91 (1980).

[43] R. Kadono, J. Imazato, T. Matsuzaki, K. Nishiyama, K. Nagamine, T. Yamazaki, D. Richter, and J.-M. Welter, Phys. Rev. B **39**, 23 (1989).

[44] G. M. Luke, J. H. Brewer, S. R. Kreitzman, D. R. Noakes, M. Celio, R. Kadono, and E. J. Ansaldo, Phys. Rev. B **43**, 3284 (1991).

[45] J. E. Hirsch and S. Tang, Phys. Rev. Lett. **62**, 591 (1989).

[46] J. Lorenzana, G. Seibold, and R. Coldea, Phys. Rev. B **72**, 224511 (2005).

[47] C. Mazzoli, G. Allodi, G. Guidi, R. De Renzi, P. Ghigna, and C. Baines, Phys. B: Condens. Matter **326**, 427 (2003).

[48] T. Lancaster, S. J. Blundell, P. J. Baker, W. Hayes, S. R. Giblin, S. E. McLain, F. L. Pratt, Z. Salman, E. A. Jacobs, J. F. C. Turner, and T. Barnes, Phys. Rev. B **75**, 220408(R) (2007).

[49] I. de Pinho Ribeiro Moreira and F. Illas, Phys. Rev. B **60**, 5179 (1999).

[50] C. Yasuda, S. Todo, K. Hukushima, F. Alet, M. Keller, M. Troyer, and H. Takayama, Phys. Rev. Lett. **94**, 217201 (2005).

[51] Data will be made available at doi:10.5286/ISIS.E.RB2010120-1.

[52] P. Giannozzi, S. Baroni, N. Bonini, M. Calandra, R. Car, C. Cavazzoni, D. Ceresoli, G. L. Chiarotti, M. Cococcioni, I. Dabo, A. D. Corso, S. de Gironcoli, S. Fabris, G. Fratesi, R. Gebauer, U. Gerstmann, C. Gougoussis, A. Kokalj, M. Lazzeri, L. Martin-Samos *et al.*, J. Phys.: Condens. Matter **21**, 395502 (2009).

[53] J. P. Perdew, K. Burke, and M. Ernzerhof, Phys. Rev. Lett. **77**, 3865 (1996).

[54] S. F. J. Cox, J. Phys. C: Solid State Phys. **20**, 3187 (1987).